

# Corrosion Resistance and Catalytic Activity toward the Oxygen Reduction Reaction of $\text{CoCrFe}_x\text{Ni}$ ( $0 \leq x \leq 0.7$ ) Thin Films

Clara Linder,\* Smita G. Rao, Robert D. Boyd, Arnaud le Febvrier, Per Eklund, Sara Munktel, and Emma M. Björk\*



Cite This: *ACS Appl. Energy Mater.* 2022, 5, 10838–10848



Read Online

ACCESS |



Metrics & More



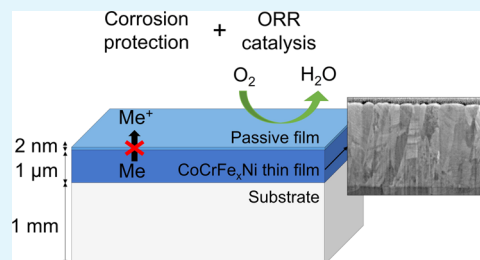
Article Recommendations



Supporting Information

**ABSTRACT:** Corrosion resistance and catalytic activity toward the oxygen reduction reaction (ORR) in an alkaline environment are two key properties for water recombination applications. In this work,  $\text{CoCrFe}_x\text{Ni}$  ( $0 \leq x \leq 0.7$ ) thin films were deposited by magnetron sputtering on polished steel substrates. The native passive layer was 2–4 nm thick and coherent to the columnar grains determined by transmission electron microscopy. The effect of Fe on the corrosion properties in 0.1 M NaCl and 1 M KOH and the catalytic activity of the films toward ORR were investigated. Electrochemical impedance spectroscopy and potentiodynamic polarization measurements indicate that  $\text{CoCrFe}_{0.7}\text{Ni}$  and  $\text{CoCrFe}_{0.3}\text{Ni}$  have the highest corrosion resistance of the studied films in NaCl and KOH, respectively. The high corrosion resistance of the  $\text{CoCrFe}_{0.7}\text{Ni}$  film in NaCl was attributed to the smaller overall grain size, which leads to a more homogeneous film with a stronger passive layer. For  $\text{CoCrFe}_{0.3}\text{Ni}$  in KOH, it was attributed to a lower Fe dissolution into the electrolyte and the build-up of a thick and protective hydroxide layer. Scanning Kelvin probe force microscopy showed no potential differences globally in any of the films, but locally, a potential gradient between the top of the columns and grain boundaries was observed. Corrosion of the films was likely initiated at the top of the columns where the potential was lowest. It was concluded that Fe is essential for the electrochemical activation of the surfaces and the catalytic activity toward ORR in an alkaline medium. The highest catalytic activity was recorded for high Fe-content films ( $x \geq 0.5$ ) and was attributed to the formation of platelet-like oxide particles on the film surface upon anodization. The study showed that the combination of corrosion resistance and catalytic activity toward ORR is possible for  $\text{CoCrFe}_x\text{Ni}$ , making this material system a suitable candidate for water recombination in an alkaline environment.

**KEYWORDS:** magnetron sputtering, multicomponent thin film, corrosion, ORR, water recombination, electrocatalysis



## INTRODUCTION

Alkaline batteries are widely used for standby and uninterrupted power supplies, which can be found, for example, in hospitals' backup generators, data centers, or industrial processes.<sup>1</sup> Industrial rechargeable batteries can be stored for more than 20 years but require periodical maintenance due to electrolyte loss as a result of water splitting. One way to tackle this issue is to add an electrocatalyst for water recombination. However, alkaline batteries are considered harsh and corrosive environments because of their high hydroxide concentration and caustic properties,<sup>2,3</sup> thus the batteries rely on corrosion-resistant materials for their durability. The corrosion resistance of metals is often achieved by their protective oxide on their surfaces, also known as the passive layer.<sup>4</sup>

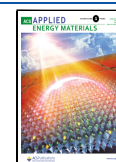
In high entropy alloys (HEA), a new class of multicomponent alloys first established by Yeh et al.<sup>5</sup> and Cantor et al.,<sup>6</sup> several elements are present in equimolar or nearly equimolar proportions. As a consequence, their entropy of mixing is high and free Gibbs energy is lowered<sup>6</sup> and this tends to enhance certain physical properties of alloys such as mechanical strength and corrosion resistance.  $\text{CoCrFeNi}$  alloys

are one of the HEA families that have been studied for their promising corrosion properties. Hsu et al.<sup>7</sup> showed that a  $\text{CoCrFeNi}$  alloy had a similar corrosion behavior to stainless steel 304L in NaCl.  $\text{CoCrNi}$  and  $\text{CoCrFeMnNi}$  even had higher corrosion resistance than stainless steel in  $\text{H}_2\text{SO}_4$ ,<sup>8–10</sup> which was attributed to the growth of a Cr-rich oxide. In NaOH, extensive dissolution of Cr was observed, which led to a porous passive film.<sup>8</sup> Impact of additions of Co,<sup>11</sup> Cu,<sup>7</sup> Mn,<sup>12</sup> Al,<sup>13</sup> and Nb<sup>14</sup> on corrosion resistance and passivity of these alloys have been reported but the effect of Fe has so far not been investigated. Fe is known to preferentially dissolve to the benefit of Cr in steels<sup>15</sup> and high entropy alloys.<sup>10,16,17</sup> Therefore, it is of interest to investigate what the critical Fe content is for the change in material properties. Because of the

Received: May 16, 2022

Accepted: August 15, 2022

Published: August 25, 2022



excellent corrosion properties of these HEAs, they have also been synthesized as coatings and thin films. CoCrFeNi and CoCrCuFeNi films synthesized by vacuum hot sintering<sup>18</sup> and CoCrFeMnNi by laser cladding<sup>19</sup> on steel and CoCrFeMnNi by electrodeposition<sup>20</sup> on copper have been reported as effectively protecting the substrates and showed similar corrosion resistance to stainless steel 304 in NaCl and in H<sub>2</sub>SO<sub>4</sub>. The corrosion properties of AlCoCrFeNi thin films deposited by RF magnetron sputtering have been studied by Gao et al.<sup>21</sup> and Shi et al.<sup>22</sup> However, the corrosion resistance in an alkaline environment is yet to be reported to ensure that the films are suitable, for instance, for an alkaline battery application.

As previously mentioned, alkaline batteries would benefit from the introduction of a water recombinant electrocatalyst to tackle water loss. The kinetically limiting reaction in water recombination is the oxygen reduction reaction (ORR), which requires an electrocatalyst. Cobalt oxides as nanoparticles have been reported to be efficient toward ORR,<sup>23,24</sup> and we have previously demonstrated that Co thin films can be used as electrocatalysts.<sup>25</sup> Other alternatives with high efficiency for ORR are Ni/NiO<sup>26</sup> and NiCo<sub>2</sub>O<sub>4</sub> spinels.<sup>27</sup>

The structural and mechanical properties of CoCrFeNi thin films deposited by magnetron sputtering have been studied by various research groups<sup>28–32</sup> but neither their corrosion properties nor their catalytic activity toward ORR has been investigated. In this study, we report the synthesis of CoCrFeNi thin films with varying Fe content by magnetron sputtering and their corrosion resistance in an alkaline environment together with their catalytic activity toward ORR. Furthermore, the effect of the Fe concentration on these properties was investigated to aid in designing a bifunctional material system.

## MATERIALS AND METHODS

**Thin-Film Deposition.** Low-alloyed carbon steel (C 0.08 wt %; Si 0.02 wt %; Mn 0.52 wt %; Al 0.04 wt %; Cr 0.04 wt %; Fe balance) 1 mm thick plates were cut into 2-in. disks, ground, and polished with diamond paste (down to particle size of 0.25  $\mu$ m). The disks were ultrasonically cleaned with ethanol. CoCrFeNi thin films were deposited by direct current magnetron sputtering. The system was equipped with four 30° inclined magnetrons<sup>33</sup> and the base pressure in the chamber was  $< 10^{-7}$  Pa. Four 50-mm-diameter elemental targets were used. The total power applied to the targets was kept constant at 400 W. Argon gas was introduced at each magnetron with a flow of 35 sccm corresponding to a process pressure of 0.3 Pa. The steel substrate was heated to 300 °C prior to the deposition. The substrate was rotated at 15 rpm during the deposition to ensure uniform deposition. The deposition time was 30 min, aiming for 1  $\mu$ m thick films.

**Structural Analysis of Thin Films.** The crystal structure of the films was characterized by X-ray diffraction (XRD) using a Bruker D8 Discover diffractometer in a symmetric  $\theta/2\theta$  configuration and a Cu K $\alpha$  X-ray source ( $\lambda = 1.5406$  Å). The morphology and chemical composition of the thin films were analyzed using a scanning electron microscope (SEM) Sigma 300 VP Gemini (Zeiss, 5 kV acceleration voltage) and an energy dispersive spectroscopy (EDS) detector (Oxford Instruments X-MAX<sup>N</sup>, 5 kV acceleration voltage) integrated into the microscope. The average grain size for the films was determined from 20 grain measurements in the SEM micrographs.

To determine the thicknesses of the films and to study their microstructure, cross-sectional samples for analysis by SEM and transmission electron microscopy (TEM) were prepared using a dual beam SEM-focused ion beam (FIB) microscope (Gemini Zeiss 1540 sB). Samples were placed with a 54° angle tilt, facing a Ga<sup>+</sup> ion source to sputter away the film. Pt layers were first deposited on top of the

film to protect the surface of the film during milling. SEM images of the cross sections were taken using the same instrument using a 36° image correction to take account of the sample tilt. Thin lamellae suitable for TEM analysis were prepared using the well-established lift-out approach. All TEM analyses were performed using an FEI Tecnai G2 TF 20 UT microscope operated at a 200 kV acceleration voltage. For scanning transmission electron microscopy (STEM), a high-angle annular detector was used spanning an angular range of 80–260 mrad.

Scanning Kelvin probe force microscopy (SKPFM) was used to measure potential maps of the samples in addition to the height maps obtained through atomic force microscopy (AFM). A Bruker Dimension Icon AFM microscope was used in the frequency modulation mode (FM-KFM). A PtIr-coated Si tip, with a 200–250  $\mu$ m length and a resonance frequency of 60–100 kHz, was used for the measurements. The results were analyzed using NanoScope analysis V1.9 software.

**Electrochemical Measurements.** To investigate their corrosion properties, the films were immersed in a neutral chloride (0.1 M NaCl) and an alkaline electrolyte (1 M KOH), and electrochemical measurements were carried out with a PARSTAT 3000A–DX potentiostat. A three-electrode setup was used where the working electrode was the thin film, a Ag/AgCl saturated with KCl ( $E = 0.197$  V vs SHE) was used as a reference electrode, and a Pt wire was used as a counter electrode. The open-circuit potential (OCP) was first measured for 30 min. Electrochemical impedance spectroscopy (EIS) was carried out at OCP. A potential difference of 10 mV was applied with frequencies from 100 kHz to 10 mHz. The data were analyzed and fitted to equivalent electronic circuits using ZSimpWin 3.60 software. The circuits consist of different components: resistors and constant phase elements (CPE). The CPE is used to model a nonideal capacitor and considers the heterogeneity at the thin-film surface. Its impedance can be written as  $Z_{CPE} = 1/[Y_0(j\omega)^n]$ , where  $Z_{CPE}$  is the impedance for the CPE,  $Y_0$  is the modulus,  $j$  is the complex number,  $\omega$  is the angular frequency, and  $n$  is the correction factor ( $n = 1$  when the capacitor is ideal and  $0.5 < n < 1$  when it is nonideal).  $R_s$  and  $R_{ct}$  are resistors that model the resistance of the solution and the charge transfer resistance, respectively. After EIS measurements, potentiodynamic polarization (PD) was carried out from  $-0.25$  V vs OCP to  $0.8$  V for NaCl and  $0.6$  V vs Ag/AgCl for KOH, with a scan rate of  $0.167$  mV/s (10 mV/min). The Tafel module in VersaStudio software was used to calculate the Tafel slopes and determine the corrosion current density  $j_{corr}$ . The extrapolation was carried out  $\pm 0.1$  V away from  $E_{corr}$ . All measurements were repeated for duplicate samples and carried out at room temperature. A wrought stainless steel 316L sample was used as a reference material in 0.1 M NaCl, as it is a well-known corrosion-resistant material in a neutral chloride environment.

Cyclic voltammetry (CV) and potentiostatic experiments for ORR catalysis testing in 1 M KOH were carried out in the same cell as for the corrosion testing. Scan rates for the initial CVs were 200 mV/s and for the ORR 5 mV/s. The resulting plots shown in Figure 8 were taken as an average value of the last three CVs for the 200 mV/s scan rate and the last CV after 10 cycles for the ORR testing at 5 mV/s. Prior to ORR testing, the electrolyte was purged with pressurized oxygen gas (O<sub>2</sub>) for 30 min to saturate the solution or with nitrogen (N<sub>2</sub>) to obtain an oxygen-free condition. To confirm that the recorded catalytic activity is related to ORR activity of the CoCrFeNi films and not due to deposited Pt from the counter electrode on the films, the ORR measurements were also carried out with a graphite counter electrode (available in the Supporting Information).

## RESULTS

**As-Deposited Thin Films.** Table 1 shows the composition of the different thin films in atomic % based on EDS measurements. The Fe content was varied from 0 to 19 at % with Co, Cr, and Ni adjusted accordingly. The films were named CoCrFe<sub>x</sub>Ni, where  $x$  is the Fe content over the average composition of Co, Cr, and Ni in the films. No notable composition gradients were observed along the film growth

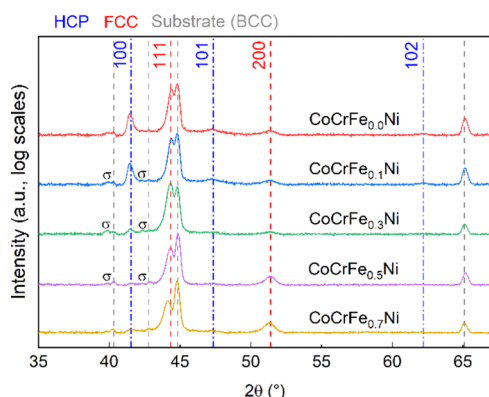


**Table 1. Elemental Composition (at %) Based on EDS Measurements of the Films**

at %	Co	Cr	Fe	Ni
CoCrFe <sub>0.0</sub> Ni	37.3 ± 0.1	28.9 ± 0.3	0	33.8 ± 0.2
CoCrFe <sub>0.1</sub> Ni	36.1 ± 0.1	28.1 ± 0.1	2.4 ± 0.2	33.4 ± 0.2
CoCrFe <sub>0.3</sub> Ni	33.7 ± 0.2	26.4 ± 0.2	8.6 ± 0.2	31.3 ± 0.1
CoCrFe <sub>0.5</sub> Ni	31.7 ± 0.2	24.9 ± 0.3	14.0 ± 0.2	29.3 ± 0.3
CoCrFe <sub>0.7</sub> Ni	29.0 ± 0.1	24.3 ± 0.3	18.9 ± 0.2	27.9 ± 0.1

direction (based on the EDS line profiling available in Supporting Information Figure S1).

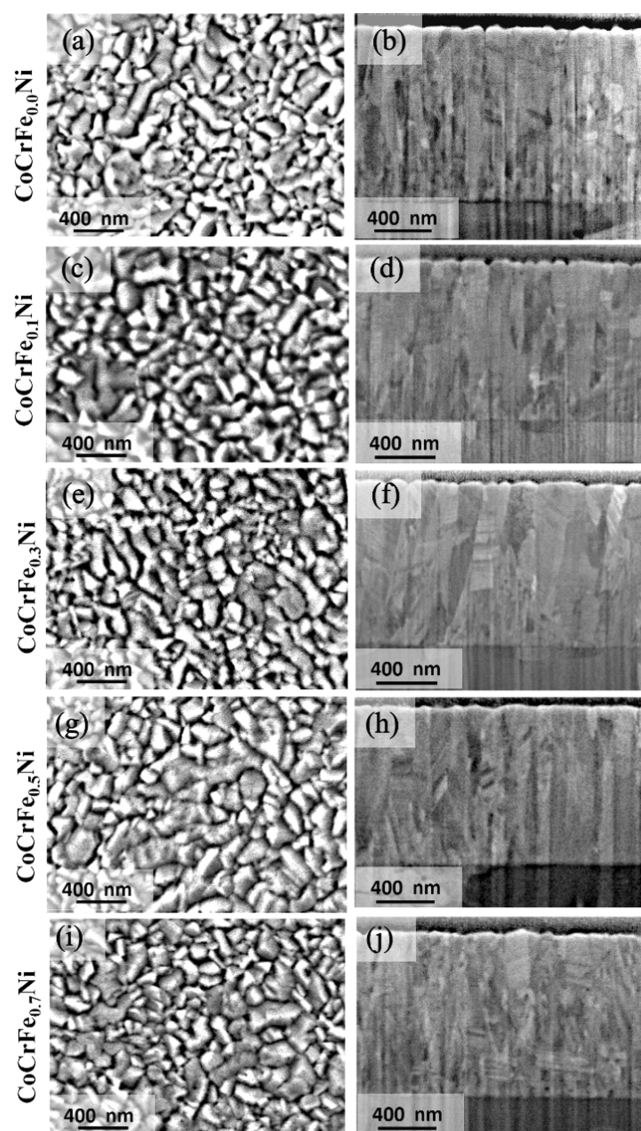
The crystal structure of the films was analyzed by XRD. The diffractograms are presented in Figure 1.

**Figure 1.** X-ray diffractograms from the films. Identified phases are represented by dashed lines or symbols ( $\sigma$  for the sigma phase).

The steel substrate has a randomly oriented, body-centered cubic (BCC) structure. For all films, three peaks can be indexed to a face-centered cubic (FCC) phase.<sup>7,28,34</sup> The relative intensity of the peaks corresponding to the 200 and 220 planes of the FCC lattice decreases when the Fe content decreases. The peak intensity for the 111 FCC plane does not seem to be affected by the composition and could indicate a small degree of texture along the [111] direction. For films with low Fe concentrations ( $x = 0$ –0.3), a hexagonal close-packed (HCP) structure is also observed.<sup>35–37</sup> The peak intensity for the HCP phase increases with decreased Fe content. The 002 plane for the HCP phase is located at  $\sim 44^\circ$  and overlaps with the FCC 111 peak. A secondary tetragonal  $P4mm$  group phase was identified for films with  $x = 0.1$ –0.5, which could be a sigma ( $\sigma$ ) phase in agreement with Kini et al.<sup>34</sup> The lattice parameters for the FCC phase calculated from the 111 plane are 3.53 Å for CoCrFe<sub>0.0</sub>Ni and 3.55 Å for CoCrFe<sub>0.7</sub>Ni, which are consistent with those of the previously reported CoCrFeNi thin film.<sup>34</sup> The lattice parameters of the HCP phase calculated from the 100 and 101 planes are  $a = 2.52$  Å and  $c = 4.05$  Å.

The surface morphology and the films' cross sections were analyzed by SEM. Figure 2 features plane-view and cross-sectional images of the deposited films.

From the plane-view images (Figure 2a,c,e,g,i), large grains ( $\sim 270$  nm in width) and smaller grains ( $< 75$  nm in diameter) can be observed. When the Fe content is decreased, the number of these large grains decreases. The measured average grain sizes for the films are 159( $\pm 76$ ), 199( $\pm 60$ ), 203( $\pm 76$ ), 244( $\pm 62$ ), and 255( $\pm 75$ ) nm for  $x = 0, 0.1, 0.3, 0.5$ , and 0.7, respectively. The cross-sectional images (Figure 2b,d,f,h,j)

**Figure 2.** SEM plane-view (a, c, e, g, i) and SEM images of the FIB prepared cross sections (b, d, f, h, j).

show that the grains are columnar and their width is consistent with the plane-view images. The columnar growth becomes less evident when the Fe content increases, indicating less defined grain boundaries and smaller grain size. Intragrain features are present within the columns seen as lines almost parallel to the substrate surface. These features are more clearly seen in the TEM images (Figure 3 column 2). The film thicknesses are consistent at  $\sim 1.1$   $\mu\text{m}$  for all films. For CoCrFe<sub>0.0</sub>Ni, a small gap between the film and the substrate is observed in the cross-sectional micrograph. This could indicate a decreased adhesion of the film to the steel substrate when no Fe is present in the film.

The cross-sectional micrographs show that the films are less columnar at the 200 nm closest to the substrate. This is further confirmed in the TEM micrographs in Figure 3 (column 1, top of grains indicated by hollow arrows) where small triangular shaped grains can be observed at the film–substrate interface. This indicates a mixed orientation competitive growth at the initial film formation. At the top of the films (Figure 3 column 2), columnar growth is dominant, and a thin (2–4 nm) oxide layer (Figure 3 column 3) is present on the surface of all grains

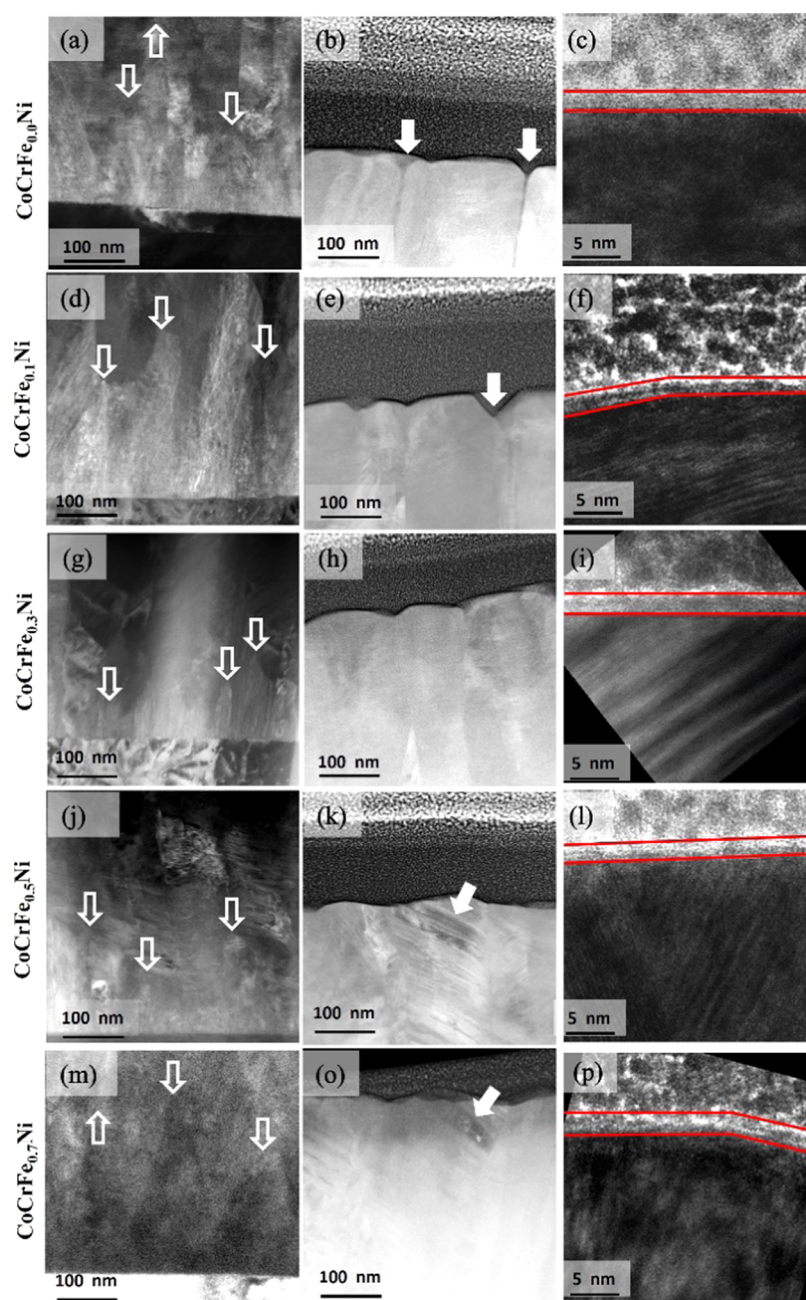


**Figure 3.** TEM micrographs of the films and HAADF-STEM of the film–substrate interface (column 1: (a, d, g, j, m)); hollow arrows indicate signs of competitive growth, and of top of the film (column 2: (b, e, h, k, o)); arrows indicate the presence of defects in the films. HRTEM of the native oxide layer indicated by red lines (column 3: (c, f, i, l, p)).

on all samples. The HRTEM images also confirm the presence of the oxide layer, which seems to be crystalline, although the exact structure or orientation could not be determined. From the STEM and HRTEM images, it appears that the number of defects increases with the Fe content. Features within the columnar grains shown by arrows in the HAADF-STEM images (Figure 3 column 2 indicated by arrows) show stacking faults and twin boundaries.<sup>34</sup> Well-defined grain boundaries are visible in the STEM images (indicated by arrows) for  $\text{CoCrFe}_{0.0}\text{Ni}$ , indicating either that they are underdense or phase separation has occurred. The fitted SAED patterns (Figure S2) indicate the presence of the HCP phase in addition to FCC for  $x = 0\text{--}0.3$  in agreement with findings from XRD analysis. For the high Fe content films, the pattern

becomes more ring-like, indicating a higher number of domains analyzed and, hence, a smaller overall grain size, as shown in SEM images.

**Corrosion Resistance.** To investigate the corrosion performances of the deposited thin films, two environments were selected: 0.1 M NaCl, pH 6 and 1 M KOH, pH 13. EIS measurements were carried out to gain information about the resistance of the passive layer.<sup>38,39</sup> Nyquist plots from EIS spectra recorded at OCP for the films and the substrate are shown in Figure 4(a) in 0.1 M NaCl and (b) in 1 M KOH.

In both environments, semicircles were recorded, one for 0.1 M NaCl and two for 1 M KOH (with the exception of  $\text{CoCrFe}_{0.0}\text{Ni}$ ); each semicircle is attributed to a layer in the passive film. To quantify the corrosion resistance, equivalent



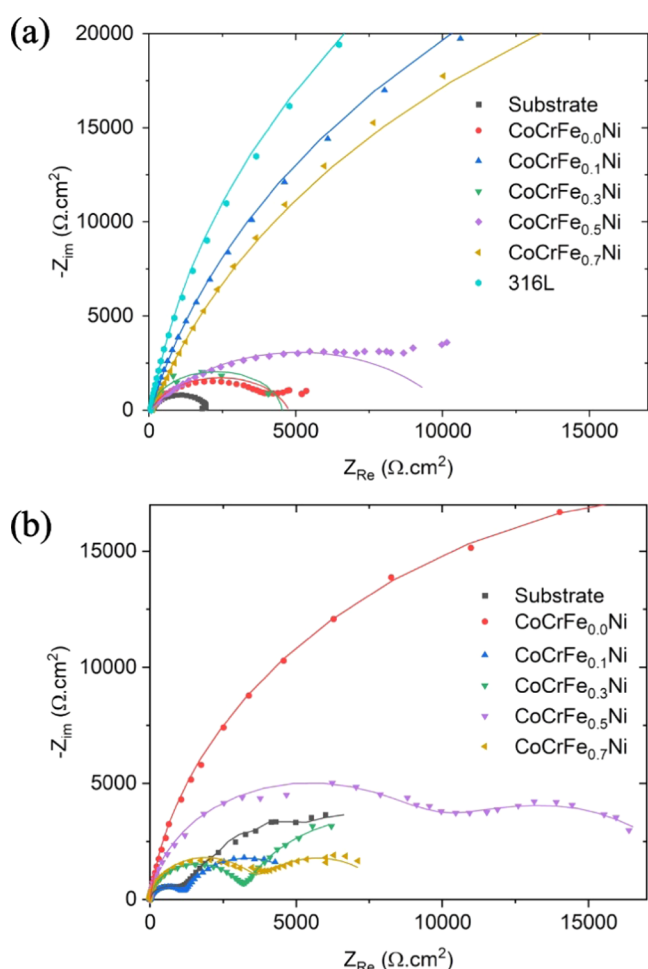


**Figure 4.** Nyquist plots for the EIS data recorded in 0.1 M NaCl (a) and 1 M KOH (b) for the films, substrate, and 316L reference. The lines correspond to the fitted model to the raw data (symbols).

electronic circuits were chosen based on prior knowledge of the passive film structure in these environments<sup>40,41</sup> and their fit to the recorded data (fitted data presented as solid lines in Figure 4 and numerically in Table 2). The selected circuits are shown in Figure 5.

The higher the resistance values ( $R_{ct}$ ,  $R_{ox}$ , and  $R_{hyd}$ ) and the lower the capacitance values ( $Y_0$ ), the higher the corrosion resistance. In NaCl, CoCrFe<sub>0.7</sub>Ni and CoCrFe<sub>0.1</sub>Ni have the highest  $R_{ct}$  amongst the films, one magnitude higher than the substrate and close to 316L, and the films also have low associated capacitance  $Y_0$ , showing that these films have the strongest, thickest, and most stable passive film.<sup>41</sup>

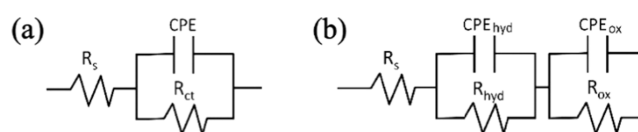


**Figure 5.** Equivalent electronic circuits used for the EIS data fitting for samples immersed in NaCl (a) and KOH (b).

In 1 M KOH, the outer layer is associated to a porous hydroxide on top of the inner oxide layer. The presence of hydroxides after immersion in KOH was also confirmed by FTIR analysis (Supporting information, Figure S3). CoCrFe<sub>0.0</sub>Ni has the highest  $R$  and low  $Y_0$  values for both hydroxide and oxide layers, which indicates that this film has the most protective and thickest oxide and hydroxide layer.<sup>40,41</sup> Small additions of Fe ( $x = 0.1$ – $0.3$ ) decrease the protectiveness of the oxide layer based on the low  $R_{ox}$  and high  $Y_{0-ox}$ <sup>41</sup> observed. By increasing the Fe content ( $x = 0.5$ – $0.7$ ), the inner oxide layer becomes more protective and denser with a small increase of  $R_{ox}$  but especially with lower  $Y_{0-ox}$  values ( $2.7 \times 10^{-5}$  on average). This could mean that for  $x > 0.5$ , the oxide layer grows underneath a more porous hydroxide layer (higher  $Y_{0-hyd}$ ).<sup>40</sup> All films have a corrosion resistance almost 10 times higher than the substrate.

Potentiodynamic polarization was applied to gain information on the corrosion onset, pitting resistance, and corrosion rate.<sup>38,42</sup> Figure 6 shows typical polarization curves in (a) 0.1 M NaCl and in (b) 1 M KOH.

In 0.1 M NaCl, all films have corrosion potentials close to each other and exhibit a passive region. The lowest corrosion current densities of the films are recorded for CoCrFe<sub>0.7</sub>Ni and CoCrFe<sub>0.1</sub>Ni. All films and 316L exhibit a pitting potential, where the current increases more rapidly, around 0.2–0.5 V for the films and 0.67 V for 316L. The formation of pits was verified by SEM imaging after the corrosion testing (Supporting Information Figure S4).

In an alkaline environment, 1 M KOH, the film's corrosion behavior differs significantly compared to that in 0.1 M NaCl. After reaching the corrosion potential, the films present a sharp peak followed by a constant current region until the critical potential is reached. The peak corresponds to an active region where the initial passive film is modified, most likely depassivated, and then reformed. The sharp increase in current is the start of the transpassive region where the passive film is further oxidized but also the onset of the oxygen evolution reaction that contributes to the current density. The corrosion current density is the lowest for CoCrFe<sub>0.0</sub>Ni and CoCrFe<sub>0.3</sub>Ni, and their depassivation potential is higher than that of the other films, indicating that reducing the Fe content improves the corrosion properties in a basic environment. However, this

**Table 2.** EIS Simulation Results with  $R_s$ ,  $R_{hyd}$ ,  $Y_{0-hyd}$ , and  $n_{hyd}$  Parameters for the Outer Hydroxide Layer Formed on Top of the Oxide Layer, which is Modeled by  $R_{ox}$ ,  $Y_{0-ox}$ , and  $n_{ox}$  for the Films and Substrate in 0.1 M NaCl and 1 M KOH

		$R_s$ ( $\Omega \cdot \text{cm}^2$ )	$R_{hyd}$ ( $\Omega \cdot \text{cm}^2$ )	$Y_{0-hyd}$ ( $\Omega^{-1} \cdot \text{cm}^{-2}$ )	$n_{hyd}$	$R_{ox}$ ( $\Omega \cdot \text{cm}^2$ )	$Y_{0-ox}$ ( $\Omega^{-1} \cdot \text{cm}^{-2}$ )	$n_{ox}$
0.1 M NaCl	substrate	103.4	N.A.			$1.6 \times 10^3$	$2.3 \times 10^{-4}$	0.86
	CoCrFe <sub>0.1</sub> Ni	84.5				$2.8 \times 10^4$	$6.9 \times 10^{-6}$	0.87
	CoCrFe <sub>0.7</sub> Ni	96.3				$2.9 \times 10^4$	$6.3 \times 10^{-6}$	0.86
	316L	79.1				$9.7 \times 10^4$	$2.9 \times 10^{-5}$	0.94
1 M KOH	substrate	2.67	$9.3 \times 10^3$	$6.2 \times 10^{-4}$	0.80	$9.9 \times 10^2$	$3.6 \times 10^{-5}$	0.98
	CoCrFe <sub>0.0</sub> Ni	2.67	$5.3 \times 10^4$	$5.2 \times 10^{-4}$	0.92	$1.8 \times 10^4$	$1.0 \times 10^{-4}$	0.97
	CoCrFe <sub>0.3</sub> Ni	2.71	$5.2 \times 10^3$	$3.0 \times 10^{-5}$	0.95	$7.0 \times 10^3$	$1.2 \times 10^{-3}$	0.79
	CoCrFe <sub>0.5</sub> Ni	2.72	$8.2 \times 10^3$	$5.3 \times 10^{-4}$	0.83	$8.3 \times 10^3$	$2.9 \times 10^{-5}$	0.86

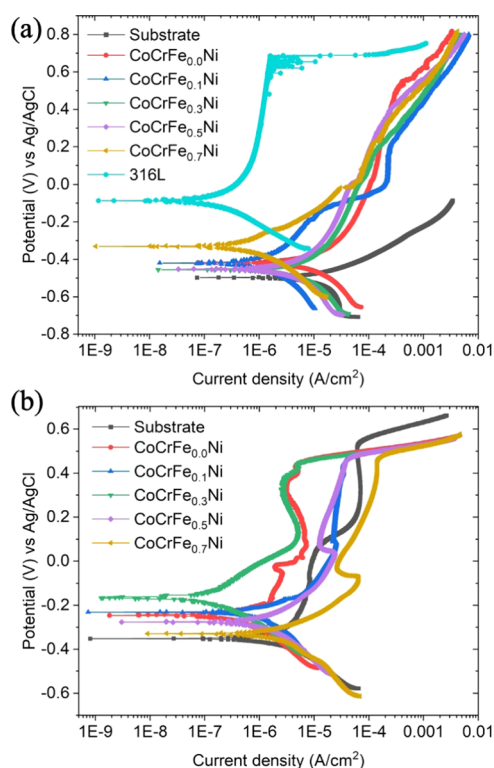


**Figure 6.** PD polarization curves for the films, substrate, and 316L in 0.1 M NaCl (a) and 1 M KOH (b) after OCP was recorded for 30 min, scan rate 10 mV/min.

trend is not observed for CoCrFe<sub>0.1</sub>Ni. Table 3 shows the extracted corrosion data in both tested environments.

The highest reduction of the corrosion current density and increase in the corrosion potential relative to the substrate are found for CoCrFe<sub>0.7</sub>Ni in NaCl (0.8 vs 17.6  $\mu\text{A}/\text{cm}^2$  and  $-0.298$  vs  $-0.559$  V). Hence, the 1.1  $\mu\text{m}$  thin film could potentially slow down the corrosion rate of the steel substrate by a factor of 22 compared to a noncoated substrate.

#### SKPFM Measurements Ex Situ after Exposure to KOH.

To further understand the surface evolution during immersion in 1 M KOH, SKPFM measurements were performed on the films as-deposited and after 30 min of immersion in KOH. The height and potential measurements for CoCrFe<sub>0.0</sub>Ni and CoCrFe<sub>0.7</sub>Ni as-deposited and after exposure to KOH are shown in Figure 7.

The maximum height differences of the film surfaces are 20–30 nm. Potential maps show that anodic regions, with the lowest potential, correspond to the top of the grains in the films. Cathodic regions, with the highest potential, are in the grain boundaries of the film. This indicates that the top of the

columnar grains is less noble in their joints, which could cause the initiation of microgalvanic corrosion. After immersion in KOH, the potential differences are less visible in the potential maps, especially in CoCrFe<sub>0.0</sub>Ni. The average potential for the films is found to be 174 and 217 mV for as-deposited CoCrFe<sub>0.0</sub>Ni and CoCrFe<sub>0.7</sub>Ni, respectively. After exposure to KOH, i.e., oxidation of the surface, the average potentials are lower, i.e.,  $-113$  and  $-107$  mV, respectively.

**Catalysis ORR Testing.** Co and Ni oxides can be active catalysts for water recombination, in particular, toward ORR in alkaline electrolytes.<sup>23,25</sup> For this purpose, the surface state of the films was assessed by CV in 1 M KOH (Figure 8a), followed by anodization to modify the films and create active oxide sites for catalysis (Figure 8b,c) and evaluation of the catalytic activity of the activated films by CV in O<sub>2</sub>-saturated 1 M KOH (Figure 8d).

The CVs in Figure 8a show two peaks, one for the anodic sweep (low to high potentials) corresponding to an oxidation reaction and one for the cathodic sweep (high to low potentials) for the reduction reaction. The sharp increase of the current at 0.55–0.60 V corresponds to the start of the oxygen evolution reaction. The anodization profiles are shown in Figure 8b; after 300 s at  $-1$  V, the potential was increased to 0.32 V to anodize the surface of the film. As a result of the potential step, the current reached a plateau and then decreases over time for CoCrFe<sub>0.7</sub>Ni and CoCrFe<sub>0.5</sub>Ni. The plateau is less evident in the other films. CoCrFe<sub>0.7</sub>Ni was further investigated with SEM after the anodization step (Figure 8c), which revealed that  $\sim 200$  nm wide and a few nm thick platelet-shaped particles had grown on the film surface. EDS analysis shows that these particles are enriched in oxygen (compared to the as-deposited film and the surrounding film after anodization), which indicates that oxide particles had formed during the anodization step.

During the ORR testing (Figure 8d), the highest cathodic current density ( $-0.2$  mA/cm<sup>2</sup>) was recorded for CoCrFe<sub>0.7</sub>Ni and CoCrFe<sub>0.5</sub>Ni. This indicates that films with a strong response during anodization are catalytically active. The ORR for these films starts around  $-0.2$  V and forms a peak at  $-0.3$  V. This region can then be used for Tafel extrapolations and extraction of kinetic constants, as summarized in Table 4. The exchange current density for the films is in the  $10^{-4}$  mA/cm<sup>2</sup> order, which is promising for the films as it is only one magnitude lower compared to that of carbon-supported Pt particles.<sup>43</sup> The Tafel slopes for the films are around  $-160$  mV/dec, which is 70 mV/dec higher than the ones reported for Pt/C catalysts<sup>43,44</sup> and CoCrFeNi nanoparticles,<sup>45</sup> indicating slightly slower kinetics for the films.

The ORR peak is followed by a current increase possibly due to continued ORR activity and the build-up of reaction

**Table 3.** Corrosion Potential  $E_{\text{corr}}$ , Corrosion Current Density  $j_{\text{corr}}$ , Pitting Potential  $E_{\text{pit}}$ , and Depassivation Potential for All Films, Substrate, and 316L Reference Obtained from the Recorded Polarization Curves

	$E_{\text{corr}}$ (V) NaCl	$j_{\text{corr}}$ ( $\mu\text{A}/\text{cm}^2$ ) NaCl	$E_{\text{pit}}$ (V) NaCl	$E_{\text{corr}}$ (V) KOH	$j_{\text{corr}}$ ( $\mu\text{A}/\text{cm}^2$ ) KOH	depassivation potential (V) KOH
substrate	$-0.559$	17.650		$-0.350$	3.181	
CoCrFe <sub>0.0</sub> Ni	$-0.469$	10.981	0.321	$-0.295$	1.736	0.116
CoCrFe <sub>0.1</sub> Ni	$-0.333$	0.925	0.260	$-0.271$	2.356	0.129
CoCrFe <sub>0.3</sub> Ni	$-0.457$	6.442	0.370	$-0.273$	1.232	0.132
CoCrFe <sub>0.5</sub> Ni	$-0.434$	3.689	0.309	$-0.294$	1.798	0.017
CoCrFe <sub>0.7</sub> Ni	$-0.298$	0.802	0.224	$-0.356$	2.436	$-0.097$
316L	$-0.076$	0.157	0.668			



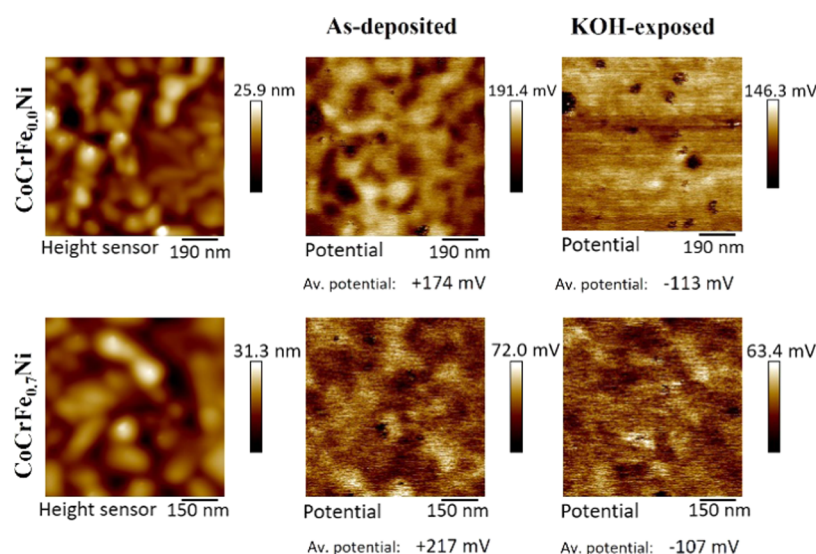


**Figure 7.** Height and potential maps of CoCrFe<sub>0.0</sub>Ni and CoCrFe<sub>0.7</sub>Ni as-deposited and after exposure to KOH.

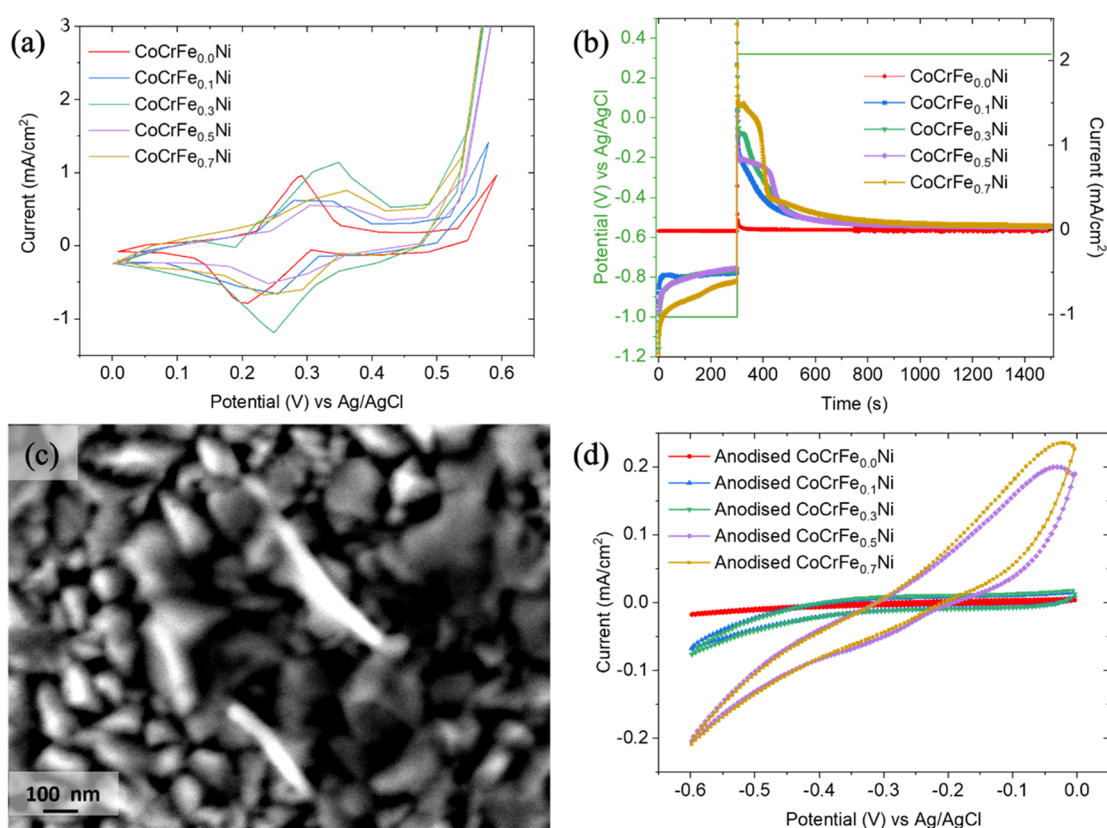


**Figure 8.** ORR catalysis study of CoCrFeNi thin films. Cyclic voltammograms (after 200 cycles) (a), anodization step to oxidize the surface (b), SEM micrograph of anodized CoCrFe<sub>0.7</sub>Ni; oxide particles are formed on top of the film (c) cyclic voltammograms in the ORR region (d).

**Table 4. Tafel Slope and Exchange Current Density Extracted from CV Measurements**

	Tafel slope (mV/dec)	exchange current density $j_0$ (mA/cm <sup>2</sup> )
CoCrFe <sub>0.5</sub> Ni	−168	$8.8 \times 10^{-4}$
CoCrFe <sub>0.7</sub> Ni	−160	$6.3 \times 10^{-4}$
Pt/C <sup>43</sup>	−90	$1.2 \times 10^{-3}$

products on the surface of the films as the sample is not rotating. In the case of a rotating disk electrode, this potential

region corresponds to the diffusion-limited region.<sup>46</sup> Prior to the ORR potential, in the surface reaction-controlled region, the current is rather high (0.2 mA/cm<sup>2</sup>), which could be due to the oxidation of the films or adsorption of oxygen molecules. To confirm that the recorded catalytic activity is related to ORR activity of the CoCrFeNi films and not due to deposited Pt from the counter electrode on the films, a control ORR measurement was performed using a graphite counter electrode (supporting information, Figure S7). No significant

changes in the catalytic activity were observed with the electrode change.

## DISCUSSION

**Film Structure.** The XRD results in Figure 1 show that all films present a major FCC phase, which is in agreement with previous studies.<sup>28–32,34</sup> For Fe content  $x \geq 0.3$ , the FCC phase is dominant, and the HCP phase is prohibited. Fe seems to have a similar role to Mn in the study by Li et al.,<sup>35</sup> where the FCC phase is stabilized. This suggests that a phase transformation from the FCC phase to HCP has occurred in the films, as the stacking sequences for HCP and FCC are close to each other.<sup>36</sup> This phase transformation has been reported for CoCrFeNi and CoCrFeMnNi alloys.<sup>36,47,48</sup> Co has a stable HCP structure;<sup>49</sup> as the films are composed of over 33 at % of Co, this could affect the phase transformation.

The small intensity peaks in the XRD spectra have been identified as a sigma phase.<sup>34</sup> Interestingly, the sigma phase is not present for the film with close to equimolar composition but is only present for low to medium Fe content ( $x = 0.1–0.5$ ). In Kini et al.'s<sup>34</sup> study, the sigma phase is believed to be Cr-enriched, which could also be the case here for the films with higher Cr contents. Both the hexagonal and sigma phase are supposedly nanosized grains and are not possible to distinguish in TEM analysis.

Adding Fe into the film seems to decrease the difference in surface energies between the film and the steel substrates, enabling the diffusion of adatoms, which form larger nuclei and later columns.<sup>50,51</sup> The triangular shapes in the first 200 nm of the film (Figures 2 and 3) are typical for competitive growth and zone model T<sup>52</sup> where two grain orientations are present at the same time until one of them takes over for the columns. Based on the XRD spectra, the two directions are [111] and [200].

The density of stacking faults and other defects increases with the Fe content in the films based on the SEM and TEM images shown in Figures 2 and 3. This could be explained by the higher lattice distortion when multiple elements are present in a structure. This has previously been observed in thin films<sup>32,53</sup> and for alloys<sup>54,55</sup> of these types of materials.

**Corrosion in NaCl.** The single phase and high density of defects seem to have a beneficial role in terms of corrosion resistance in NaCl, as CoCrFe<sub>0.7</sub>Ni has the highest resistance, based on EIS and PD results. The less defined columnar structure in CoCrFe<sub>0.7</sub>Ni suggests that the film has a finer grain structure and is more nanocrystalline compared to CoCrFe<sub>0.3</sub>Ni, where the columns and grain boundaries are more defined. It has been reported for Co–Cr coatings<sup>56</sup> and other alloys<sup>57</sup> that nanosized grains have a higher corrosion resistance compared to coarse grains. The higher density of grain boundaries in nanograined structures leads to a more uniform material with less compositional differences between the interior of grains and grain boundaries.

The presence of the HCP phase in the CoCrFe<sub>0.0</sub>Ni phase could be the reason for the film's lower corrosion resistance in NaCl as it can create a galvanic cell with the main FCC phase.<sup>58</sup> The presence of secondary phases has been reported for HEA alloys as detrimental to the corrosion properties.<sup>7,13,59</sup> Since no Fe is present in CoCrFe<sub>0.0</sub>Ni, a pure Cr oxide would form in the passive film and is likely not as resistant as it would with Fe additions. For stainless steel, the passive film is often multilayered with an inner Cr–Fe oxide and an outer Cr hydroxide layer.<sup>60</sup>

**Corrosion in KOH.** The EIS measurements in KOH indicate that a hydroxide layer on top of the film's native oxide layer was formed (Figure 4b and Supporting Information Figure S3). CoCrFe<sub>0.3</sub>Ni and CoCrFe<sub>0.0</sub>Ni have the highest corrosion resistance based on EIS and PD results. The high resistivity and low capacitance for CoCrFe<sub>0.0</sub>Ni reveal a highly protective and thick passive layer, which leads to a low corrosion current density (Table 3). This could be due to higher chemical stability due to the lack of dissolution of Fe in KOH.<sup>61</sup> The formation of the hydroxide layer is believed to be the result of the continuous diffusion of metallic cations from the bulk toward the film surface. The depassivation peak observed in the PD measurements (Figure 6b and Table 3) at around 0.1 V vs Ag/AgCl corresponds to the potential region where Cr<sub>2</sub>O<sub>3</sub> is further oxidized to CrO<sub>4</sub><sup>2–</sup>.<sup>3,62</sup> This implies that the passive film is first dissolved in the electrolyte and then reformed. For low Fe-containing films, this depassivation occurs at higher potentials and a small second peak can be observed at around 0.4 V just before the transpassive region. The second peak is in agreement with the study of Ni alloys by Mishra et al.<sup>62</sup> where Cr and Mo are depleted and a Ni(OH)<sub>2</sub> layer is formed. The films with no Fe or low content consequentially have a higher Ni content compared to the other films; this could mean that the higher depassivation potential is due to the Cr dissolution and Ni activity.

The Volta potential maps obtained by SKPFM (Figure 7) indicate no major difference within the films on the micrometer scale but rather on the nanometer scale. These potential differences could be due to uneven passive film thickness, localized and superficial chemical gradients (not detected by EDS mapping), or amounts of free atoms or electrons available to be oxidized. The difference before and after KOH exposure is more significant for CoCrFe<sub>0.0</sub>Ni compared to CoCrFe<sub>0.7</sub>Ni. This suggests that in the absence of Fe, the film has a higher ability to be homogeneously oxidized; in the presence of Fe, the high density of defects hinders the oxidation. Based on the Volta potential obtained for the films and the SKPFM measurements after exposure to KOH, the anodic regions in the as-deposited films are first to be oxidized, resulting in a decreased potential difference after immersion to KOH, which indicates the formation of an even passive layer. SKPFM analysis of AlCoCrFeNi alloys has previously shown that potential differences between phases were the initiation points for corrosion.<sup>13,63</sup> This is however interpreted for individual grains in the present study.

**Catalytic Activity.** The CVs in Figure 8a show that the anodic peak slightly shifts toward higher potential when the Fe content is increased in the films, indicating that the overpotential for the oxidation of the surface species increases with the Fe content. Nevertheless, the average activation potential is around 0.32 V and is likely to correspond to the oxidation of Co<sup>2+</sup> and Ni<sup>2+</sup> to Co<sup>3+</sup> and Ni<sup>3+</sup>, respectively.<sup>64,65</sup> This potential is then used for the anodization to promote the oxidation of these species and form active sites for electrocatalysis. Based on the Pourbaix diagrams, the reaction taking place could be the formation of cobalt spinel Co<sub>3</sub>O<sub>4</sub> and nickel hydroxide Ni(OH)<sub>2</sub><sup>66</sup> or a mix of both.<sup>67</sup> Cr and Fe do not have any characteristic redox reaction at this potential; however, Wang et al.<sup>67</sup> reported in their simulated Pourbaix diagrams the formation of NiFe<sub>2</sub>O<sub>4</sub> in addition to Co<sub>3</sub>O<sub>4</sub> and Ni(OH)<sub>2</sub>, indicating that Fe can be involved in the reaction as well. The current plateau is more evident for CoCrFe<sub>0.7</sub>Ni and CoCrFe<sub>0.3</sub>Ni, indicating that more of the film is oxidized and



that Fe plays a role here. After the formation of the double-layered passive film, Fe cations are likely to be present in the film and provide a higher electron transfer and oxidation rate of the films.<sup>68</sup> Similar behavior has been reported by Torbati-Sarrafi et al.<sup>12</sup> where Mn enhanced the diffusion of oxygen vacancies in CoCrFeNiMn due to the formation of a more defective passive film.

Once the surfaces were activated, the films were tested as catalysts for ORR. Similarly, to the anodization step, CoCrFe<sub>0.7</sub>Ni and CoCrFe<sub>0.5</sub>Ni had the highest current densities. The catalytic activity in the films is attributed to the Co<sup>3+</sup> and Ni<sup>3+</sup> active sites in the anodized surfaces as it has been reported in other studies<sup>26,65,69,70</sup> and also in our study about Co thin films<sup>25</sup> but also to the synergy effect with Fe additions. Higher catalytic activity toward OER and ORR when Fe is introduced in excess in FeNi<sub>3</sub>/NC nanoparticles has been reported by Chen et al.<sup>68</sup> Nevertheless, the high performance of the films was hypothesized to be due to the lattice distortion caused by the addition of Fe, which increases the surface area and the density of active sites. The authors also report that the excess of Fe cations provides more active electrons in the overall electronic structure, which enhances the electron transfer and thus increases the catalytic effect. Higher Tafel slopes and lower exchange current densities were found for the anodized films compared to Pt/C catalysts. This is likely due to the lower surface area available for the films compared to nanoparticles; however, this could be tailored to enhance the CoCrFeNi thin films further.

## CONCLUSIONS

CoCrFe<sub>x</sub>Ni thin films with varying Fe contents were successfully deposited with magnetron sputtering on low alloy steel substrates. It was observed that Fe stabilizes the FCC structure of the film, while films with a Fe content  $x \leq 0.3$  have a secondary HCP phase. However, the higher the Fe content, the more defects are present in the films, and overall smaller grain size was observed.

In 0.1 M NaCl, the films with high Fe content ( $x = 0.7$ ) had the highest corrosion resistance. The high resistance is attributed to less defined columnar grains and higher defect density, which lead to the formation of a more protective passive film. In 1 M KOH, the medium Fe content ( $x = 0.3$ ) presented the lowest corrosion current density and higher resistance of the passive layer. The higher performances are related to the lower Fe content and dissolution rate into the electrolyte and the build-up of a thick and protective hydroxide layer. A potential difference between the top of the grains and grain boundaries was observed, which could be due to passive film thickness and local superficial chemical gradient.

Anodization of thin films resulted in the formation of platelet-shaped particles grown on the surface of films with high Fe content. These particles were found to be active toward ORR, and the highest activity was recorded for high Fe content films. Fe enhanced the electron transfer at the active Co<sup>3+</sup> and Ni<sup>3+</sup> sites, making these films promising electrocatalysts in an alkaline medium.

The combination of corrosion resistance and catalytic activity toward ORR is possible for CoCrFe<sub>x</sub>Ni ( $x \geq 0.5$ ), as the corrosion current densities remained low and the catalytic activity high, making this material system a suitable candidate for water recombination in an alkaline environment.

## ASSOCIATED CONTENT

### Supporting Information

The Supporting Information is available free of charge at <https://pubs.acs.org/doi/10.1021/acsaem.2c01499>.

EDS line profiles and maps for CoCrFe<sub>0.7</sub>Ni, SAED fitted patterns, FTIR-IRRAS spectra for as-deposited and KOH immersed films, complete EIS simulation results for NaCl and KOH corrosion testing, SEM micrograph of a corrosion pit after immersion into NaCl, SKPFM height and potential maps for CoCrFe<sub>0.1–0.3</sub>Ni, CVs from ORR testing in O<sub>2</sub> and N<sub>2</sub> purged KOH solutions, CV from ORR testing with Pt and graphite rod as a counter electrode, and CVs from ORR testing on the as-deposited Co-enriched CoCrFeNi film (PDF)

## AUTHOR INFORMATION

### Corresponding Authors

**Clara Linder** — RISE, Corrosion, Vehicles and Surface Protection, 164 40 Kista, Sweden; Nanostructured Materials Division, Department of Physics, Chemistry and Biology (IFM), Linköping University, 581 83 Linköping, Sweden; [orcid.org/0000-0003-0611-3324](https://orcid.org/0000-0003-0611-3324); Email: [clara.linder@liu.se](mailto:clara.linder@liu.se)

**Emma M. Björk** — Nanostructured Materials Division, Department of Physics, Chemistry and Biology (IFM), Linköping University, 581 83 Linköping, Sweden; [orcid.org/0000-0001-6609-6779](https://orcid.org/0000-0001-6609-6779); Email: [emma.bjork@liu.se](mailto:emma.bjork@liu.se)

### Authors

**Smita G. Rao** — Thin Film Physics Division, Department of Physics, Chemistry, and Biology (IFM), Linköping University, 581 83 Linköping, Sweden

**Robert D. Boyd** — Nanostructured Materials Division, Department of Physics, Chemistry and Biology (IFM), Linköping University, 581 83 Linköping, Sweden; [orcid.org/0000-0002-6602-7981](https://orcid.org/0000-0002-6602-7981)

**Arnaud le Febvrier** — Thin Film Physics Division, Department of Physics, Chemistry, and Biology (IFM), Linköping University, 581 83 Linköping, Sweden; [orcid.org/0000-0002-3059-7392](https://orcid.org/0000-0002-3059-7392)

**Per Eklund** — Thin Film Physics Division, Department of Physics, Chemistry, and Biology (IFM), Linköping University, 581 83 Linköping, Sweden; [orcid.org/0000-0003-1785-0864](https://orcid.org/0000-0003-1785-0864)

**Sara Munktel** — Swerim AB, Metallic materials in corrosive environments, 164 40 Kista, Sweden

Complete contact information is available at: <https://pubs.acs.org/doi/10.1021/acsaem.2c01499>

### Funding

This study was performed within the Competence Centre FunMat-II and was funded by the Swedish Agency for Innovation Systems (VINNOVA, grant no 2016-05156, and grant no 2019-04881). The authors would also like to acknowledge the Swedish Government Strategic Research Area in Materials Science on Functional Materials at the Linköping University (Faculty Grant SFO-Mat-LiU No. 2009 00971). The Centre in Nanoscience and Nanotechnology at LiTH (CeNano) at the Linköping University is also acknowledged. P. E. and A. I. F. also acknowledge the Swedish Research Council under project number 2021-03826.

## Notes

The authors declare no competing financial interest.

## REFERENCES

- (1) Beaudin, M.; Zareipour, H.; Schellenberg, A.; Rosehart, W. Energy Storage for Mitigating the Variability of Renewable Electricity Sources. *Energy Storage Smart Grids Plan. Oper. Renew. Var. Energy Resour.* **2015**, 1–33.
- (2) Insitute Nickel Development, I. *Corrosion Resistance of the Austenitic Chromium-Nickel Stainless Steels in Chemical Environments*, 1963.
- (3) Davalos Monteiro, R.; van de Wetering, J.; Krawczyk, B.; Engelberg, D. L. Corrosion Behaviour of Type 316L Stainless Steel in Hot Caustic Aqueous Environments. *Met. Mater. Int.* **2020**, 26, 630–640.
- (4) Jones, D. A. *Principles and Prevention of Corrosion: Pearson New International Edition*, 2nd ed.; Prentice Hall, 1996; Vol. 14.
- (5) Yeh, J. W.; Chen, S. K.; Lin, S. J.; Gan, J. Y.; Chin, T. S.; Shun, T. T.; Tsau, C. H.; Chang, S. Y. Nanostructured High-Entropy Alloys with Multiple Principal Elements: Novel Alloy Design Concepts and Outcomes. *Adv. Eng. Mater.* **2004**, 6, 299–303.
- (6) Cantor, B.; Chang, I. T. H.; Knight, P.; Vincent, A. J. B. Microstructural Development in Equiatomic Multicomponent Alloys. *Mater. Sci. Eng.* **2004**, 375–377, 213–218.
- (7) Hsu, Y. J.; Chiang, W. C.; Wu, J. K. Corrosion Behavior of FeCoNiCrCu High-Entropy Alloys in 3.5% Sodium Chloride Solution. *Mater. Chem. Phys.* **2005**, 92, 112–117.
- (8) Wang, J.; Li, W.; Yang, H.; Huang, H.; Ji, S.; Ruan, J.; Liu, Z. Corrosion Behavior of CoCrNi Medium-Entropy Alloy Compared with 304 Stainless Steel in H<sub>2</sub>SO<sub>4</sub> and NaOH Solutions. *Corros. Sci.* **2020**, 177, 108973.
- (9) Moravcik, I.; Sadat, N.; Motallebzadeh, A. Materials Characterization Interstitial Nitrogen Enhances Corrosion Resistance of an Equiatomic CoCrNi Medium-Entropy Alloy in Sulfuric Acid Solution. *Mater. Charact.* **2021**, 172, 110869.
- (10) Wang, L.; Mercier, D.; Zanna, S.; Seyeux, A.; Laurent-Brocq, M.; Perrière, L.; Guillot, I.; Marcus, P. Study of the Surface Oxides and Corrosion Behaviour of an Equiatomic CoCrFeMnNi High Entropy Alloy by XPS and ToF-SIMS. *Corros. Sci.* **2020**, 167, No. 108507.
- (11) Zhao, R. F.; Ren, B.; Cai, B.; Liu, Z. X.; Zhang, G. P.; Zhang, J. jian. Corrosion Behavior of CoCrCuFeMnNi High-Entropy Alloys Prepared by Hot Pressing Sintered in 3.5% NaCl Solution. *Results Phys.* **2019**, 15, No. 102667.
- (12) Torbati-Sarraf, H.; Shabani, M.; Jablonski, P. D.; Pataky, G. J.; Poursae, A. The Influence of Incorporation of Mn on the Pitting Corrosion Performance of CrFeCoNi High Entropy Alloy at Different Temperatures. *Mater. Des.* **2019**, 184, No. 108170.
- (13) Shi, Y.; Collins, L.; Feng, R.; Zhang, C.; Balke, N.; Liaw, P. K.; Yang, B. Homogenization of AlCoCrFeNi High-Entropy Alloys with Improved Corrosion Resistance. *Corros. Sci.* **2018**, 133, 120–131.
- (14) Wang, W.; Qi, W.; Xie, L.; Yang, X.; Li, J.; Zhang, Y. Microstructure and Corrosion Behavior of (CoCrFeNi)<sub>95</sub>Nb<sub>5</sub> High-Entropy Alloy Coating Fabricated by Plasma Spraying. *Materials* **2019**, 12, 694.
- (15) Jung, R. H.; Tsuchiya, H.; Fujimoto, S. XPS Characterization of Passive Films Formed on Type 304 Stainless Steel in Humid Atmosphere. *Corros. Sci.* **2012**, 58, 62–68.
- (16) Dai, C.; Luo, H.; Li, J.; Du, C.; Liu, Z.; Yao, J. X-Ray Photoelectron Spectroscopy and Electrochemical Investigation of the Passive Behavior of High-Entropy FeCoCrNiMox Alloys in Sulfuric Acid. *Appl. Surf. Sci.* **2020**, 499, No. 143903.
- (17) Lou, Y.; Dai, C.; Chang, W.; Qian, H.; Huang, L.; Du, C.; Zhang, D. Microbiologically Influenced Corrosion of FeCoCrNi-Mo<sub>0.1</sub> High-Entropy Alloys by Marine *Pseudomonas Aeruginosa*. *Corros. Sci.* **2020**, 165, 108390.
- (18) Shang, C.; Axinte, E.; Ge, W.; Zhang, Z.; Wang, Y. High-Entropy Alloy Coatings with Excellent Mechanical, Corrosion Resistance and Magnetic Properties Prepared by Mechanical Alloying and Hot Pressing Sintering. *Surf. Interfaces* **2017**, 9, 36–43.
- (19) Ye, Q.; Feng, K.; Li, Z.; Lu, F.; Li, R.; Huang, J.; Wu, Y. Microstructure and Corrosion Properties of CrMnFeCoNi High Entropy Alloy Coating. *Appl. Surf. Sci.* **2017**, 396, 1420–1426.
- (20) Yoosefan, F.; Ashrafi, A.; Monir vaghefi, S. M. Characterization of Co–Cr–Fe–Mn–Ni High-Entropy Alloy Thin Films Synthesized by Pulse Electrodeposition: Part 2: Effect of Pulse Electrodeposition Parameters on the Wettability and Corrosion Resistance. *Met. Mater. Int.* **2020**, 27, 106.
- (21) Gao, L.; Liao, W.; Zhang, H.; Surjadi, J. U.; Sun, D.; Lu, Y. Microstructure, Mechanical and Corrosion Behaviors of CoCrFeNiAl 0.3 High Entropy Alloy (HEA) Films. *Coatings* **2017**, 7, 156.
- (22) Shi, Y.; Yang, B.; Rack, P. D.; Guo, S.; Liaw, P. K.; Zhao, Y. High-Throughput Synthesis and Corrosion Behavior of Sputter-Deposited Nanocrystalline Alx(CoCrFeNi)100-x Combinatorial High-Entropy Alloys. *Mater. Des.* **2020**, 195, No. 109018.
- (23) Li, Y.; Li, Q.; Wang, H.; Zhang, L.; Wilkinson, D. P.; Zhang, J. Recent Progresses in Oxygen Reduction Reaction Electrocatalysts for Electrochemical Energy Applications. *Electrochem. Energy Rev.* **2019**, 2, 518–538.
- (24) Liang, Y.; Wang, H.; Diao, P.; Chang, W.; Hong, G.; Li, Y.; et al. Oxygen Reduction Electrocatalyst Based on Strongly Coupled Cobalt Oxide Nanocrystals and Carbon Nanotubes. *J. Am. Chem. Soc.* **2012**, 134, 15849–15857.
- (25) Linder, C.; Rao, S. G.; le Febvrier, A.; Greczynski, G.; Sjövall, R.; Munktel, S.; Eklund, P.; Björk, E. M. Cobalt Thin Films as Water-Recombination Electrocatalysts. *Surf. Coatings Technol.* **2020**, 404, 126643.
- (26) Liu, P.; Ran, J.; Xia, B.; Xi, S.; Gao, D.; Wang, J. Bifunctional Oxygen Electrocatalyst of Mesoporous Ni/NiO Nanosheets for Flexible Rechargeable Zn–Air Batteries. *Nano-Micro Lett.* **2020**, 12, 68.
- (27) Liu, Z. Q.; Xu, Q. Z.; Wang, J. Y.; Li, N.; Guo, S. H.; Su, Y. Z.; Wang, H. J.; Zhang, J. H.; Chen, S. Facile Hydrothermal Synthesis of Urchin-like NiCo<sub>2</sub>O<sub>4</sub> Spheres as Efficient Electrocatalysts for Oxygen Reduction Reaction. *Int. J. Hydrogen Energy* **2013**, 38, 6657–6662.
- (28) Savan, A.; Allermann, T.; Wang, X.; Grochla, D.; Banko, L.; Kalchev, Y.; Kostka, A.; Pfetzing-Micklich, J.; Ludwig, A. Structure Zone Investigation of Multiple Principle Element Alloy Thin Films as Optimization for Nanoindentation Measurements. *Materials* **2020**, 13, 2113.
- (29) Nagy, P.; Rohbeck, N.; Roussely, G.; Sortais, P.; Lábár, J. L.; Gubicza, J.; Michler, J.; Pethő, L. Processing and Characterization of a Multibeam Sputtered Nanocrystalline CoCrFeNi High-Entropy Alloy Film. *Surf. Coatings Technol.* **2020**, 386, No. 125465.
- (30) Chawake, N.; Zálesák, J.; Gammer, C.; Franz, R.; Cordill, M. J.; Kim, J. T.; Eckert, J. Microstructural Characterization of Medium Entropy Alloy Thin Films. *Scr. Mater.* **2020**, 177, 22–26.
- (31) Cao, F.; Munroe, P.; Zhou, Z.; Xie, Z. Microstructure and Mechanical Properties of a Multilayered CoCrNi/Ti Coating with Varying Crystal Structure. *Surf. Coatings Technol.* **2018**, 350, 596–602.
- (32) Huo, W.; Liu, X.; Tan, S.; Fang, F.; Xie, Z.; Shang, J.; Jiang, J. Ultrahigh Hardness and High Electrical Resistivity in Nano-Twinned, Nanocrystalline High-Entropy Alloy Films. *Appl. Surf. Sci.* **2018**, 439, 222–225.
- (33) le Febvrier, A.; Landalv, L.; Liersch, T.; Sandmark, D.; Sandstrom, P.; Eklund, P. An Upgraded Ultra-High Vacuum Magnetron-Sputtering System for High-Versatility and Software-Controlled Deposition. *Vacuum* **2021**, 187, No. 110137.
- (34) Kini, M. K.; Lee, S.; Savan, A.; Breitbach, B.; Addab, Y.; Lu, W.; Ghidelli, M.; Ludwig, A.; Bozzolo, N.; Scheu, C.; Chatain, D.; Dehm, G. Nanocrystalline Equiatomic CoCrFeNi Alloy Thin Films: Are They Single Phase Fcc. *Surf. Coatings Technol.* **2021**, 410, No. 126945.
- (35) Li, Z.; Pradeep, K. G.; Deng, Y.; Raabe, D.; Tasan, C. C. Metastable High-Entropy Dual-Phase Alloys Overcome the Strength-Ductility Trade-Off. *Nature* **2016**, 534, 227–230.



- (36) Tracy, C. L.; Park, S.; Rittman, D. R.; Zinkle, S. J.; Bei, H.; Lang, M.; Ewing, R. C.; Mao, W. L. High Pressure Synthesis of a Hexagonal Close-Packed Phase of the High-Entropy Alloy CrMnFeCoNi. *Nat. Commun.* **2017**, *8*, No. 15634.
- (37) Cao, F.; Munroe, P.; Zhou, Z.; Xie, Z. Medium Entropy Alloy CoCrNi Coatings: Enhancing Hardness and Damage-Tolerance through a Nanotwinned Structuring. *Surf. Coatings Technol.* **2018**, *335*, 257–264.
- (38) Kelly, R. G.; Scully, J. R.; Shoesmith, D.; Buchheit, R. G. *Electrochemical Techniques in Corrosion Science and Engineering*, 2002.
- (39) Bard, A. J.; Faulkner, L. R. *Electrochemical Methods: Fundamentals and Applications*, 2nd ed.; Bard, A. J.; Faulkner, L. R., Eds.; 2001.
- (40) Cui, Z.; Wang, L.; Ni, H.; Hao, W.; Man, C.; Chen, S.; Wang, X.; Liu, Z.; Li, X. Influence of Temperature on the Electrochemical and Passivation Behavior of 2507 Super Duplex Stainless Steel in Simulated Desulfurized Flue Gas Condensates. *Corros. Sci.* **2017**, *118*, 31–48.
- (41) Chen, T.; John, H.; Xu, J.; Lu, Q.; Hawk, J.; Liu, X. Influence of Surface Modifications on Pitting Corrosion Behavior of Nickel-Base Alloy 718. Part I: Effect of Machine Hammer Peening. *Corros. Sci.* **2013**, *77*, 230–245.
- (42) Nyby, C.; Guo, X.; Saal, J. E.; Chien, S.-C.; Gerard, A. Y.; Ke, H.; Li, T.; Lu, P.; Oberdorfer, C.; Sahu, S.; Li, S.; Taylor, C. D.; Windl, W.; Scully, J. R.; Frankel, G. S. Electrochemical Metrics for Corrosion Resistant Alloys. *Sci. Data* **2021**, *8*, 1–11.
- (43) Beyhan, S.; Şahin, N. E.; Pronier, S.; Léger, J. M.; Kadirgan, F. Comparison of Oxygen Reduction Reaction on Pt/C, Pt-Sn/C, Pt-Ni/C, and Pt-Sn-Ni/C Catalysts Prepared by Bönemann Method: A Rotating Ring Disk Electrode Study. *Electrochim. Acta* **2015**, *151*, 565–573.
- (44) Xiao, J.; Kuang, Q.; Yang, S.; Xiao, F.; Wang, S.; Guo, L. Surface Structure Dependent Electrocatalytic Activity of Co<sub>3</sub>O<sub>4</sub> Anchored on Graphene Sheets toward Oxygen Reduction Reaction. *Sci. Rep.* **2013**, *3*, No. 2300.
- (45) Löffler, T.; Meyer, H.; Savan, A.; Wilde, P.; Garzón Manjón, A.; Chen, Y. T.; Ventosa, E.; Scheu, C.; Ludwig, A.; Schuhmann, W. Discovery of a Multinary Noble Metal-Free Oxygen Reduction Catalyst. *Adv. Energy Mater.* **2018**, *8*, 1802269.
- (46) Wang, J.; Zhao, C. X.; Liu, J. N.; Ren, D.; Li, B. Q.; Huang, J. Q.; Zhang, Q. Quantitative Kinetic Analysis on Oxygen Reduction Reaction: A Perspective. *Nano Mater. Sci.* **2021**, *3*, 313–318.
- (47) Benson, M. L.; Liaw, P. K.; Choo, H.; Brown, D. W.; Daymond, M. R.; Klarstrom, D. L. Strain-Induced Phase Transformation in a Cobalt-Based Superalloy during Different Loading Modes. *Mater. Sci. Eng. A* **2011**, *528*, 6051–6058.
- (48) Fang, W.; Chang, R.; Ji, P.; Zhang, X.; Liu, B.; Qu, X.; Yin, F. Transformation Induced Plasticity Effects of a Non-Equal Molar Co-Cr-Fe-Ni High Entropy Alloy System. *Metals* **2018**, *8*, 369.
- (49) Lizárraga, R.; Pan, F.; Bergqvist, L.; Holmström, E.; Gercsi, Z.; Vitos, L. First Principles Theory of the Hcp-Fcc Phase Transition in Cobalt. *Sci. Rep.* **2017**, *7*, No. 3778.
- (50) Michely, T.; Krug, J. Condensation, Diffusion and Nucleation. In *Islands, Mounds and Atoms*, 2004; pp 13–59.
- (51) Ohring, M. *Materials Science of Thin Films*, 2002.
- (52) Greene, J. E. *Thin Film Nucleation, Growth, and Microstructural Evolution: An Atomic Scale View*, 2010.
- (53) Wu, Z. F.; Wang, X. D.; Cao, Q. P.; Zhao, G. H.; Li, J. X.; Zhang, D. X.; Zhu, J. J.; Jiang, J. Z. Microstructure Characterization of Al<sub>x</sub>Co<sub>1</sub>Cr<sub>1</sub>Cu<sub>1</sub>Fe<sub>1</sub>Ni<sub>1-x</sub> (x = 0 and 2.5) High-Entropy Alloy Films. *J. Alloys Compd.* **2014**, *609*, 137–142.
- (54) Uporov, S.; Bykov, V.; Pryanichnikov, S.; Shubin, A.; Uporova, N. Effect of Synthesis Route on Structure and Properties of AlCoCrFeNi High-Entropy Alloy. *Intermetallics* **2017**, *83*, 1–8.
- (55) Wang, S.; Zha, Y.; Hou, H. Study on the Mechanical Properties and Corrosion Resistance of Al<sub>x</sub>CoFeNiCr<sub>1-x</sub> High-Entropy Alloys. *Mater. Res. Express* **2019**, *6*, 1265e2.
- (56) Cheng, D.; Tellkamp, V. L.; Lavernia, C. J.; Lavernia, E. J. Corrosion Properties of Nanocrystalline Co-Cr Coatings. *Ann. Biomed. Eng.* **2001**, *29*, 803–809.
- (57) Ralston, K. D.; Fabijanic, D.; Biribilis, N. Effect of Grain Size on Corrosion of High Purity Aluminium. *Electrochim. Acta* **2011**, *56*, 1729–1736.
- (58) Shi, Y.; Collins, L.; Balke, N.; Liaw, P. K.; Yang, B. In-Situ Electrochemical-AFM Study of Localized Corrosion of Al<sub>x</sub>CoCrFeNi High-Entropy Alloys in Chloride Solution. *Appl. Surf. Sci.* **2018**, *439*, 533–544.
- (59) Ayyagari, A.; Hasannaeimi, V.; Grewal, H.; Arora, H.; Mukherjee, S. Corrosion, Erosion and Wear Behavior of Complex Concentrated Alloys: A Review. *Metals* **2018**, *8*, 603.
- (60) Olsson, C. O. A.; Landolt, D. Passive Films on Stainless Steels - Chemistry, Structure and Growth. *Electrochim. Acta* **2003**, *48*, 1093–1104.
- (61) Armstrong, R. D.; Baurhoo, I. The Dissolution of Iron in Concentrated Alkali. *J. Electroanal. Chem. Interfacial Electrochem.* **1972**, *40*, 325–338.
- (62) Mishra, A. K.; Shoesmith, D. W. The Activation/Depassivation of Nickel-Chromium-Molybdenum Alloys: An Oxyanion or a pH Effect - Part II. *Electrochim. Acta* **2013**, *102*, 328–335.
- (63) Xiang, C.; Zhang, Z. M.; Fu, H. M.; Han, E. H.; Zhang, H. F.; Wang, J. Q. Microstructure and Corrosion Behavior of AlCoCrFeNiSi<sub>0.1</sub> High-Entropy Alloy. *Intermetallics* **2019**, *114*, 106599.
- (64) Zhao, N.; Fan, H.; Zhang, M.; Ma, J.; Zhang, W.; Wang, C.; Li, H.; Jiang, X.; Cao, X. Investigating the Large Potential Window of NiCo<sub>2</sub>O<sub>4</sub> Supercapacitors in Neutral Aqueous Electrolyte. *Electrochim. Acta* **2019**, *321*, No. 134681.
- (65) Zhang, N.; Feng, X.; Rao, D.; Deng, X.; Cai, L.; Qiu, B.; Long, R.; Xiong, Y.; Lu, Y.; Chai, Y. Lattice Oxygen Activation Enabled by High-Valence Metal Sites for Enhanced Water Oxidation. *Nat. Commun.* **2020**, *11*, No. 4066.
- (66) Cassir, M.; Mendoza, L.; Chivot, J.; Pauporté, T.; Mansour, C. New Insight in the Behaviour of Co-H<sub>2</sub>O System at 25–150 °C, Based on Revised Pourbaix Diagrams. *Corros. Sci.* **2007**, *50*, 62–69.
- (67) Wang, K.; Han, J.; Gerard, A. Y.; Scully, J. R.; Zhou, B. C. Potential-PH Diagrams Considering Complex Oxide Solution Phases for Understanding Aqueous Corrosion of Multi-Principal Element Alloys. *npj Mater. Degrad.* **2020**, *4*, 35.
- (68) Chen, K.; Kim, S.; Rajendiran, R.; Prabakar, K.; Li, G.; Shi, Z.; Jeong, C.; Kang, J.; Li, O. L. Enhancing ORR/OER Active Sites through Lattice Distortion of Fe-Enriched FeNi<sub>3</sub> Intermetallic Nanoparticles Doped N-Doped Carbon for High-Performance Rechargeable Zn-Air Battery. *J. Colloid Interface Sci.* **2021**, *582*, 977–990.
- (69) Xu, J.; Gao, P.; Zhao, T. S. Non-Precious Co<sub>3</sub>O<sub>4</sub> Nano-Rod Electrocatalyst for Oxygen Reduction Reaction in Anion-Exchange Membrane Fuel Cells. *Energy Environ. Sci.* **2012**, *5*, 5333–5339.
- (70) Menezes, P. W.; Indra, A.; Gonza, D.; Sahraie, N. R.; Zaharieva, I.; Schwarze, M.; Strasser, P.; Dau, H.; Driess, M. High-Performance Oxygen Redox Catalysis with Multifunctional Cobalt Oxide Nano-chains: Morphology-Dependent Activity. *ACS Catal.* **2015**, *5*, 2017–2027.